THE JOURNAL OF PHYSICAL CHEMISTRY C

Article

pubs.acs.org/JPCC

Borane–Aluminum Surface Interactions: Enhanced Fracturing and Generation of Boron–Aluminum Core–Shell Nanoparticles

Jiang Yu,[†] Jerry A. Boatz,[‡] Xin Tang,[§] Zachary A. Hicks,[§] Kit H. Bowen,[§] and Scott L. Anderson*[,†]

[†]Department of Chemistry, University of Utah, 315 S 1400 E, Salt Lake City, Utah 84112, United States

[‡]Propellants Branch, Rocket Propulsion Division, Aerospace Systems Directorate, Air Force Research Laboratory, AFMC AFRL/RQRP, 10 East Saturn Boulevard, Edwards AFB, California 93524, United States

[§]Department of Chemistry, Johns Hopkins University, Baltimore, Maryland 21218, United States

Supporting Information

ABSTRACT: We present an experimental and theoretical study of borane–aluminum surface interactions that lead to rapid production of aluminum nanoparticles when Al balls are milled in the presence of diborane or pentaborane. Mass spectrometry was used to probe reactions of the boranes with aluminum fracture surfaces produced by milling collisions, which also generate local, transient high temperatures. Density functional theory was used to examine the interactions between a model aluminum surface and diborane and pentaborane, providing insight into the energetics of the first steps in the process that ultimately enables nanoparticle production. Further insight into the surface chemistry was obtained by analyzing the nanoparticles with X-ray photoelectron spectroscopy, scanning transmission electron microscopy with both electron-energy-loss and energy-dispersive X-ray spectroscopies, and dynamic light scattering. Particles were found to have fcc aluminum cores, capped by a ∼2-nm-thick shell, rich in both boron and hydrogen. The shell partially protects the aluminum from air oxidation, and further capping of the particles with organic ligands renders the particles air-stable and confers dispersibility in hydrocarbon solvents.

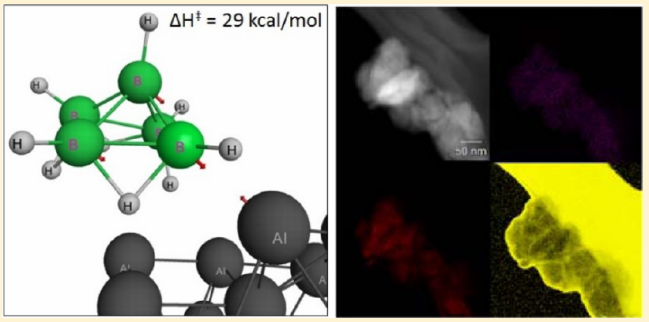

1. INTRODUCTION

Micrometer-scale aluminum is extensively used in propellants and explosives because of its high volumetric heat of combustion (∼81 kJ/mL, compared to <40 kJ/mL for typical hydrocarbons).[1−5] There is interest in further reducing the particle size to enhance ignition and combustion rates,[6−12] but the native oxide layer that forms on aluminum upon air exposure not only retards ignition but also makes up an increasing fraction of the mass as the particle size shrinks.[10,13] We have been exploring the use of mechanical attrition of aluminum in controlled environments for the high-rate production of aluminum nanoparticles, with the goal of producing particles capped with a surface layer that modifies the oxidation properties.[14−16] In this process, solid aluminum balls are milled together with a liquid or gaseous agent. As nanoscale cracks form during collisions between the balls, the milling agent reacts with the crack surfaces, reducing the surface free energy and thus enhancing crack propagation and particle production. One observation is that gaseous agents are particularly effective at both the production of particles and the production of nanoscale, rather than micrometer-scale, powder. For example, aluminum milled in liquid acetonitrile generates a ∼50:50 mixture of micro- and nanoparticles, whereas upon milling in acetonitrile vapor, only nanoparticles are produced and at a higher rate.[16] The chemistry occurring during milling can be unusual, because high instantaneous temperatures are generated in the milling collisions.

In this work, we explore the use of two boranes as milling agents. There are several reasons that borane-capped aluminum nanoparticles might be interesting. Boron and boranes are also high-energy-density materials; thus, adding borane functionality to the particle surface should not degrade energetics but could provide a means to control the surface chemistry. Specifically, we previously showed that hydrogen-terminated boron nanoparticles can be functionalized by both terminal alkenes and several ionic liquids (ILs), capping the particles with layers that prevent oxidation upon air exposure and also conferring solubility in hydrocarbons and ILs.[17,18] For alkenes, binding was attributed to the reaction of the terminal double bond with a surface B–H group, and the obvious question is whether aluminum particles produced with boranes might also have B–H surface groups that could be used to bind capping agents such as alkenes.

As shown herein, both diborane (B_2H_6) and pentaborane (B_5H_9) act as agents for rapid aluminum nanoparticle production, although the chemical properties of the particles

Received: April 16, 2017
Revised: June 9, 2017
Published: June 15, 2017

DOI: 10.1021/acs.jpcc.7b03583
J. Phys. Chem. C 2017, 121, 14176−14190

are quite different. Mass spectrometry was used to probe the chemistry during milling, and a combination of methods was used to characterize the particle size and surface chemistry. The particles were found to have aluminum cores with a thin boron- and hydrogen-rich outer layer that partially protects the Al core during air exposure. The particles can be further capped with a ligand layer (1-octene or oleic acid) that binds on the surface, rendering the particles air-stable. To help understand the chemistry occurring during milling, as freshly created aluminum surfaces interact with the boranes, density functional theory was used to examine the structures and energetics of surface complexes that are likely to form.

2. EXPERIMENTAL METHODOLOGY

2.1. Borane Reagents. Diborane was obtained as a mixture in Ar, with a nominal B_2H_6 concentration of 8.35% (Air Products). To assess the effects of milling with a higher-nuclearity boron precursor, a few experiments were performed with pentaborane (B_5H_9, Callery Chemical Company). To our knowledge, pentaborane is no longer available commercially, but we obtained an old tank that contained a small amount of liquid pentaborane.

2.2. Particle Production. As produced, the particles described below are pyrophoric, and all handling and storage of unpassivated particles was done under inert atmospheres. Aluminum nanoparticles were produced by mechanical attrition from 8-mm-diameter aluminum balls using a Retsch PM400 planetary mill operated at 350 rpm (~25.5*g* relative centrifugal force). Aluminum balls (200 g) were added to a 250 mL tungsten carbide-lined milling jar with a modified stainless steel lid equipped with valved ports. The ports allow the jar to be connected to a gas/vacuum manifold inside a N_2-filled glovebox, so that the jar can be filled with the desired milling reagents and the jar headspace can be sampled periodically during the milling process. After the Al balls had been added and the jar sealed, the jar was evacuated to 20 mTorr and refilled three times with 60 psia of Ar (99.9999%) to remove N_2 from the jar. The headspace volume of the ball-filled jar was ~175 mL.

For diborane experiments, the jar was then evacuated and pressurized with 60 psia of a nominal 8.35% mixture of diborane in Ar, sealed, loaded into the mill, and milled for 15 min at 350 rpm, which was found to result in the consumption of essentially all of the diborane. This evacuation/diborane introduction/milling process was repeated two to three times to produce the desired mass of particles. In some experiments, we first produced particles by milling aluminum balls in diborane and then remilled the particles in diborane using tungsten carbide (WC) balls at 300 rpm. The idea was to increase the B/Al ratio in the particles and reduce the particle size by reacting additional diborane with a fixed mass of aluminum nanoparticles. Two grams of particles was milled with 120 g of WC balls under 60 psia of the diborane mixture at 300 rpm.

Because the amount of pentaborane available was small and neat pentaborane is quite hazardous, our protocol was designed to minimize handling and disposal. The milling jar was filled with Al balls, the jar and gas manifold were purged with Ar and evacuated, and then the jar was connected directly to the liquid port on the pentaborane cylinder. The expectation was that this would draw mostly vapor from the nearly empty cylinder, filling the jar with at least the saturation vapor pressure of pentaborane (~200 Torr),[19] along with any other gases present in the tank headspace (e.g., N_2, originally used to pressurize the tank). Initial milling runs were short, and the jar headspace was sampled to assess the pentaborane consumption rate. For production runs, the jar was simply milled for 6 h, using a milling cycle consisting of 10-min milling periods separated by 5-min rest/cooling periods; thus, the total milling time was 4 h.

A series of runs was performed with each borane (five for diborane, three for pentaborane) to build up a stock of nanoparticle product. Visually, the amount of product in each run appeared to be quite consistent, including a mass of loose powder and additional powder adhering to the balls and jar walls. The per-run production estimates given below were determined by weighing the product, including as much of the powder adhering to the surfaces of the balls and jar walls as possible. Because processing had to be done in a glovebox, separation of the adhering material from the balls was quite tedious and was done for only a single run for each borane. In other runs, the adhering material was allowed to remain in the jar for the next run.

Some of the Al balls used in this study had been used in a previous study of nanoparticle production in acetonitrile vapor.[16] Prior to milling with any new reactant, we cleaned the balls (and milling jar) by milling them several times with the new reactant to attrite the surface layer and discarding the products. Between runs, the balls were stored in the N_2 glovebox to minimize surface oxidation. The as-received Al balls had a uniform 8-mm diameter, but because of particle attrition during use, the size decreased, and new balls were added as needed to keep the total mass of Al balls constant at 200 g. Balls smaller than ~4 mm were removed, so a distribution of diameters ranging from ~4 to 8 mm was typically present. We performed one mill run using a set of new 8-mm-diameter balls to test the effects of ball size and uniformity on the attrition process. There was no noticeable change in either the particle mass generated or the reactivity or other properties of the resulting particles.

2.3. Mass Analysis. Gases were sampled from the jar headspace into a glass vial, which was then connected to a vacuum system that housed a quadrupole mass spectrometer (SRS, RGA-200). Gases were leaked into the vacuum system to a pressure of 1×10^{-7} Torr, as measured by an ionization gauge, and mass spectra were recorded. The spectra were corrected by subtraction of a spectrum of the vacuum system background, taken each day prior to the introduction of samples. The sensitivity as a function of mass was corrected by measuring mass spectra for H_2, CH_4, Ne, ethane, ethylene, and Ar, correcting for the sensitivity of the ionization gauge to each gas. Additional details are provided in the Supporting Information.

2.4. Ligand Coating. To apply a ligand layer, particles were retrieved from the milling jar and then coated with the ligand by either simply mixing the ligand and particles by ultrasonication or by mix milling. Both procedures resulted in air-stable particles. As an example of the first procedure, a sample of particles was stirred with excess oleic acid in a glass vial to form a homogeneous paste and then ultrasonicated for 30 min, with all handling done under N_2. For mix milling, $^1/_8$-in. tungsten carbide balls were added to a sample of particles in an 80:1 mass ratio, with 2.5 mL of the ligand added per gram of particles. The objective was to thoroughly mix the sample and disrupt weakly bound aggregates while minimizing the creation of new Al surface area. Different mix-milling speeds and times were examined, and the sample discussed below was of particles prepared by milling Al balls in diborane and then subsequently

DOI: 10.1021/acs.jpcc.7b03583
J. Phys. Chem. C 2017, 121, 14176−14190

capped with 1-octene by mix milling at 300 rpm for 1 h. To retrieve the particles, 50 mL of hexane was added to the jar after mix milling, and the jar was then milled for an additional 3 h at low speed (100 rpm) to disperse the particles in the solvent.

To remove excess capping agent from the particles, samples were washed by being suspended in hexanes, centrifuged out of suspension, and then ultrasonically redispersed in fresh hexanes. This process was executed three times to remove ligands that were not bound to the particles. All liquid reagents used in processing of the particles were degassed by freeze−pump−thaw cycles or by sparging with N_2.

2.5. Particle Size and Morphology. Particle size and morphology were examined by a combination of dynamic light scattering (DLS) and scanning transmission electron microscopy (S/TEM) with energy-dispersive X-ray spectroscopy (EDS) and electron-energy-loss spectroscopy (EELS). DLS data were obtained using a NICOMP 380 particle sizing system with particles suspended in hexane. The Utah JEOL JEM 2800 S/TEM instrument is equipped with dual EDS detectors and was used to image particles in STEM dark-field mode and to produce elemental maps. An aberration-corrected S/TEM instrument with EELS capability was used at Argonne National Laboratory to examine one sample. Samples for microscopy were suspended in hexanes, drop-cast onto holey carbon TEM grids, and then air-dried overnight before analysis.

2.6. X-ray Photoelectron Spectroscopy (XPS). A Kratos Axis Ultra instrument was used to measure XPS spectra, probing the surface composition and oxidation states of the particles. The samples were prepared by being suspended in hexanes and then drop-cast onto a copper shim to form a thin layer, which was dried and then placed into the glovebox load-lock chamber and evacuated to ∼100 mTorr overnight. The samples were then transferred in air to the XPS instrument and pumped overnight in the instrument load-lock chamber at pressures below 10^{-6} Torr, before being transferred into the analysis chamber (10^{-9} Torr) for XPS analysis. Spectra were collected using a monochromatic Al Kα source (1486.7 eV) and an analysis area of 300 × 700 μm. Sample charging was compensated using the instrument's neutralizer. Data were analyzed using the CASA XPS program, and the energy scale was corrected for charging by setting the C 1s peak for adventitious carbon to 284.5 eV.

2.7. Safety Considerations. As-produced boron/aluminum nanoparticles are pyrophoric—explosively so in the case of particles produced with pentaborane. Therefore, all handling of such particles was done in a nitrogen-filled glovebox, and the particles were stored under nitrogen in glass vials that were kept in the glovebox. For experiments that required air exposure, the particles were passivated either by the ligand capping procedures discussed above or by slow exposure to a few Torr of air in the glovebox load-lock chamber. Until a particular batch of particles was confirmed to be air-stable, testing was confined to small samples and done away from combustible materials. Drying of solvent-wetted particles can result in ignition after significant delays; thus, potentially particle-contaminated materials were stored in a fume hood away from other combustibles until they were thoroughly dry. All materials were held dry for at least several days while exposed to air in a fume hood, with stirring to break up aggregates, prior to disposal as chemical waste. Diborane and pentaborane themselves are toxic and pyrophoric. Pentaborane, which was handled neat, required particular caution because it can ignite and detonate over a wide concentration range in air.

3. THEORETICAL METHODOLOGY

To gain a more detailed understanding of the interactions of diborane and pentaborane with aluminum nanoparticles, density functional theory (DFT) calculations were used to predict and characterize the structures, binding energies, and reactions of B_2H_6 and B_5H_9 on the surface of a large aluminum cluster. The theoretical approach used here is the same as that used in previous studies of aluminum nanoparticle generation utilizing simple amines[15] and acetonitrile[16] as milling agents. Briefly, an 80-atom aluminum cluster, which presents a variety of surface sites and is sufficiently large to have a small, bulk-like core, was used as a model for the surface of aluminum nanoparticles. The structures, binding energies, and selected fragmentation reaction pathways of borane molecules on the surface of Al_{80} were computed using the M06 hybrid metageneralized gradient approximation (meta-GGA) exchange-correlation functional[20] with a Lebedev quadrature grid of 99 radial and 590 angular points. The McLean−Chandler (12s,9p)/[6s,5p] basis set,[21] augmented with d-type polarization[22] and diffuse s + p functions,[23] was used for aluminum, and the 6-311++G(d,p) basis[24] was used for boron and hydrogen. For simplicity, this combination of functional and basis set is hereafter denoted as M06/6-311++G(d,p). Unless otherwise noted, all reported structures were verified as local minima or transition states by diagonalization of the Hessian matrix (i.e., the mass-weighted energy second derivatives with respect to nuclear displacements). Intrinsic reaction coordinate (IRC) calculations[25] to trace the minimum-energy pathway connecting each transition state to reactants and products were completed. Relative energies include zero-point vibrational energy (ZPVE) corrections, using a factor of 0.983[20] to scale the harmonic frequencies. All calculations were performed using the GAMESS quantum chemistry program.[26,27]

The goal of these calculations was to gain insight into the chemistry of diborane and pentaborane on the aluminum nanoparticle surface. Specifically, we wanted to understand the generation of H_2 as a gas-phase byproduct, identify borohydride species likely to be present on the nanoparticle surface, and understand the relative reactivity of pentaborane-milled nanoparticles in comparison to the diborane-milled counterparts. The strategy employed was to first consider physical and chemical binding of a single B_2H_6 or B_5H_9 molecule on the Al_{80} surface. This was followed by a systematic mapping of reactions of the physisorbed or chemisorbed molecule on the cluster surface, including B−H and, in the case of diborane, B−B fragmentation pathways. Finally, several possible pathways leading to the formation of H_2 were calculated, including "bimolecular" elimination of H_2 from adjacent chemisorbed species. Of particular interest were the predicted reaction barriers, with the relative barrier heights taken as qualitative indicators of reaction probability.

4. RESULTS AND DISCUSSION

4.1. Experimental Results. *4.1.1. Particle Production by Milling with Diborane.* We previously showed that dry milling Al balls in inert gases or liquids simply polishes them, with no significant particle generation.[14−16] Indeed, it is expected that, absent a reactive milling agent, particles are likely to be

DOI: 10.1021/acs.jpcc.7b03583
J. Phys. Chem. C 2017, 121, 14176−14190

destroyed through cold welding into large aggregates or reattachment to the ball surfaces. Therefore, it was important to know how rapidly diborane was consumed under milling conditions, and for this reason, the jar headspace gases were sampled periodically for mass spectrometric analysis during initial experiments. Figure 1 compares 70 eV electron impact

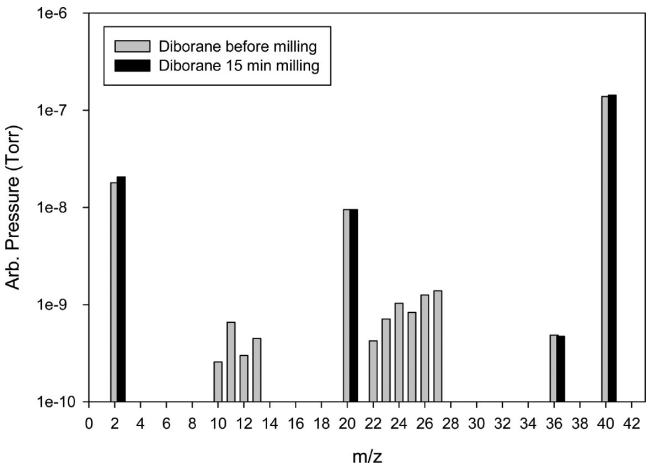

Figure 1. Headspace analysis of a diborane-milled sample before and after milling.

ionization (EI) mass spectra of the B_2H_6/Ar gas mixture as injected into the milling jar and the headspace gases sampled after 15 min of milling. To compensate for any differences in the gas sampling in the pre- and postmilling spectra, both were normalized to a constant intensity for mass 20 (Ar^{2+}, which was less likely to be saturated than Ar^+).

Consider the premilling spectrum, which was taken to assess the actual composition of the diborane gas mixture. The spectrum is dominated by peaks for masses 40, 36, and 20 from argon and a large peak for mass 2 (H_2). There are also substantial peaks in the ranges of 10−13 and 22−27 Da, which match the NIST-tabulated (70 eV EI) spectrum for diborane,[28] within the signal-to-noise ratio of the experiment. As shown in Table S1 and associated discussion, the mass 2 peak is substantially larger than expected from dissociative EI of B_2H_6,[29−31] indicating the presence of H_2 in the gas mixture, presumably generated by B_2H_6 decomposition in the gas tank. The mass spectrum shows no evidence of species other than Ar, B_2H_6, and H_2; that is, the decomposition produced no volatile products other than H_2. We previously found that milling aluminum balls in Ar or H_2 atmospheres results in no gas consumption or particle production;[15] thus, the Ar and H_2 in our Ar/H_2/B_2H_6 mixture are simply inert diluents.

As discussed in the Supporting Information, fitting of the reactant mass spectrum in Figure 1 gave the composition of the diborane reactant mixture as 4.75% B_2H_6 and 10.2% H_2, with the balance Ar. This implies that, of the 8.35% diborane present when the gas mixture was prepared, ∼3.6% had decomposed. If decomposition were to $2B_s + 3H_2$, we would expect ∼10.8% H_2 in the tank, in reasonable agreement with the observed composition. In the following discussion, we assume a diborane content of 4.75% in calculating the boron stoichiometry of our samples.

In the headspace spectrum after 15 min of milling, the peaks due to diborane are absent, and the mass 2 intensity has increased slightly (note the logarithmic scale), indicating complete diborane consumption by reaction/adsorption on the aluminum surfaces, accompanied by production of H_2. Complete diborane consumption is desirable from the perspective of efficient use of a costly reactant, as well as from safety considerations, allowing the jar headspace to simply be pumped out after milling. Using the same analysis process as was used to fit the premilling mass spectrum, we found that the H_2 concentration in the final headspace gas was only 12.1%, implying that only ∼11% of the hydrogen present in the B_2H_6 reactant was converted to gaseous H_2. Thus, all of the boron and most of the hydrogen were converted to nonvolatile form, presumably bound to the nanoparticle products.

Typically, the milling cycle—namely, evacuation of the jar, filling with fresh diborane mixture, and 15 min of milling—was repeated to build up the desired quantity of nanopowder. For a total of two cycles, ∼2 g of dry black powder was recovered, with additional powder adhering to the balls. Given a 4.75% diborane concentration in the gas mixture, each filling of the jar corresponds to 1.4 mmol of diborane; thus, two fillings introduced ∼60 mg of boron, and the resulting powder should be ∼3 wt % or ∼7 mol % boron (i.e., the B/Al mole ratio was ∼0.077). For particles with a size equivalent to ∼50-nm spheres (see below), the surface area would be ∼45 m^2/gram; thus, we estimate that ∼19 B_2H_6 molecules (∼38 B atoms) were consumed in creating each square nanometer of particle surface area. At its bulk density, solid boron has ∼25 B atoms per square nanometer of surface area, so the diborane consumed amounts to roughly 1.5 monolayers' worth of boron, but as shown by the mass spectrum, the surface layer also contained most of the hydrogen from the diborane.

Because additional aluminum particles continued to be produced in repeated cycles of milling Al balls in diborane, simply running additional fill/mill cycles did not necessarily result in a significant increase in the B/Al ratio in the product. Furthermore, the product of this type of milling always includes some particles newly attrited from the balls, as well as particles that have been milled for some time after their initial creation. Therefore, in some experiments, the particles were recovered after two fill/mill cycles and remilled for 1 h under 60 psia of the diborane gas mixture using ∼3-mm tungsten carbide balls, rather than Al balls. Because the headspace volume was greater with the denser WC balls, the boron mass in the fill was ∼41 mg of boron, increasing the boron concentration to ∼5 wt % or ∼11 mol % (B/Al mole ratio ≈ 0.13).

4.1.2. Particle Production by Milling with Pentaborane. If the pentaborane fill contained only the vapor pressure, that would equal ∼2 mmol of B_5H_9, corresponding to ∼3.5 times as many boron atoms as were present in a 60 psia fill of ∼4.75% diborane. Given that the diborane was completely consumed within 15 min of milling, our first pentaborane experiment was stopped after 30 min of milling, the jar headspace was sampled for mass analysis, and then the jar was opened for visual inspection. The aluminum balls were found to be covered with dark gray powder that appeared to be damp, indicating that some liquid pentaborane had been drawn into the jar and was not consumed within 30 min of milling. The mass spectrum in Figure S3 shows a pattern of peaks in the 10−64 Da range that are a good match to the literature spectrum for pentaborane,[28] as might be expected given that liquid was present. Mass 28 is elevated because of residual N_2 from the charge originally used to pressurize the tank, but the spectrum is dominated by a large mass 2 peak. We were unable to find literature pentaborane mass spectra extending below mass 10; thus, it is unclear how

DOI: 10.1021/acs.jpcc.7b03583
J. Phys. Chem. C 2017, 121, 14176−14190

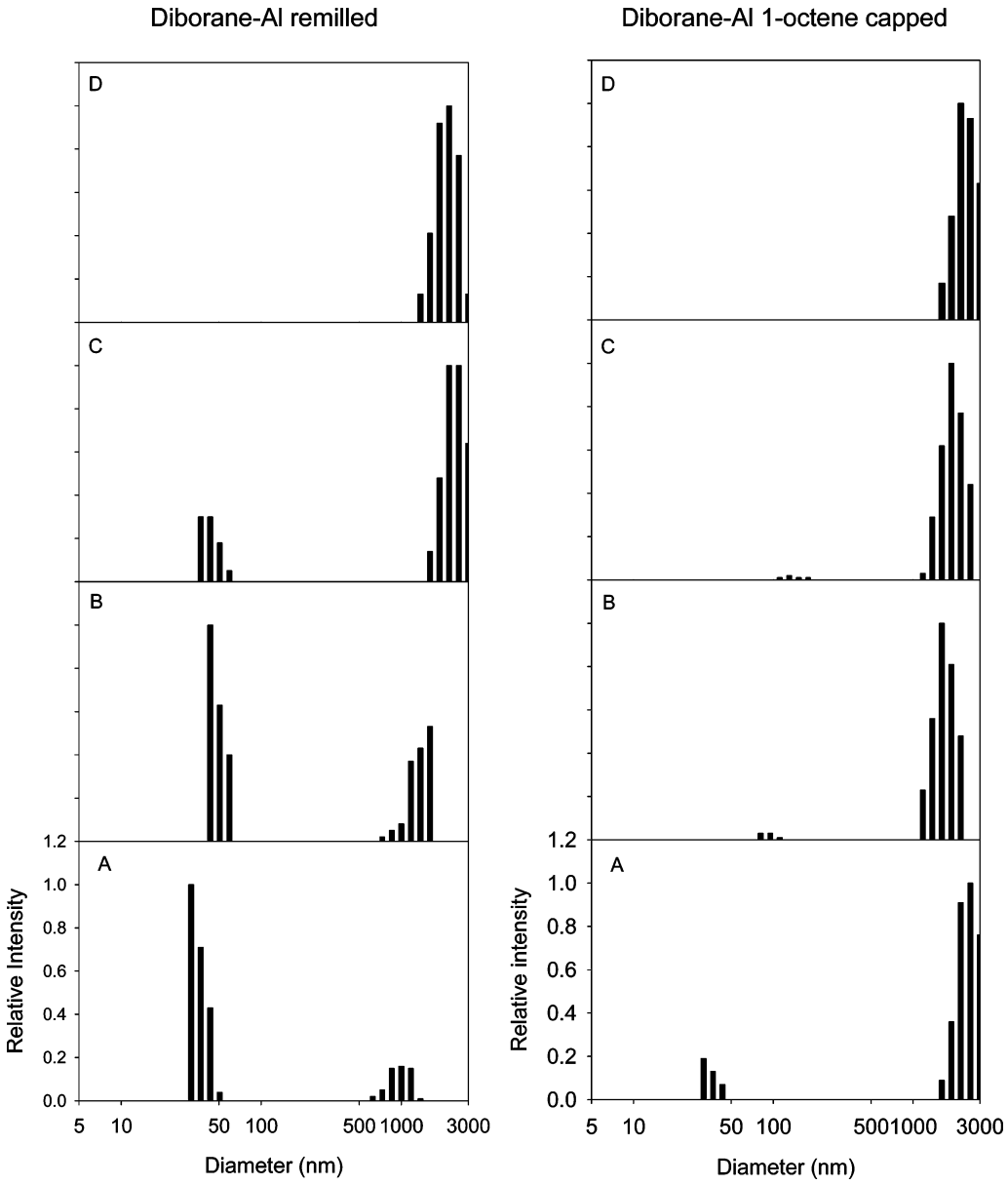

Figure 2. Dynamic light scattering (DLS) data showing the size distributions of diborane-milled aluminum nanoparticles (left) remilled in diborane with WC balls and (right) milled with 1-octene at 300 rpm.

much of the mass 2 peak comes from the dissociative ionization of B_5H_9 and how much is due to the presence of H_2 in the gas tank. In a second set of experiments, the jar was filled as before, and then the headspace was sampled and analyzed after 1.5 and 2 h of milling, without the jar being opened. As shown in Figures S4 and S5, pentaborane vapor was clearly still present, and milling was continued for a total of 4 h, to try to bring the concentration to a nonhazardous level.

Comparison of the spectra recorded at 0.5, 1.5, and 2 h provides insight into the tank gas composition. Note that the H_2 signal increased by a factor of >3 and the pentaborane concentration decreased substantially between the 1.5- and 2-h samples, demonstrating that milling with aluminum consumed pentaborane and generated H_2, as might be expected from the analogous behavior of diborane. On the other hand, there was clearly substantially less N_2 and H_2 present in the headspace at 1.5 h in experiment two, compared experiment one after 0.5 h. Our interpretation is as follows. Before the first experiment, the pentaborane tank must have had a high H_2 pressure as well as some N_2, in addition to liquid pentaborane. Because the milling jar volume was comparable to the tank volume, our initial fill in the first experiment would have substantially drawn down the H_2 and N_2 pressures in the tank, reducing the amounts of both in the fills for the second and later experiments. The amount of pentaborane remaining in the tank would also have been lower, but as will be shown below, it is clear that some liquid remained and continued to be aspirated into the milling jar.

After a total milling time of 4 h, the jar was opened in the glovebox for recovery of the milled product—a dry black powder. In several additional milling runs under these conditions (but without headspace gas sampling), between 2.5 and 3 g of a dry black powder was recovered, with additional powder adhering to the ball surfaces. If the jar were filled only with saturated pentaborane vapor, then the fill would correspond to 0.11 g of boron, and the boron concentration in the product would be ~3.7 wt % or ~9 mol % (B/Al mole ratio

DOI: 10.1021/acs.jpcc.7b03583
J. Phys. Chem. C 2017, 121, 14176−14190

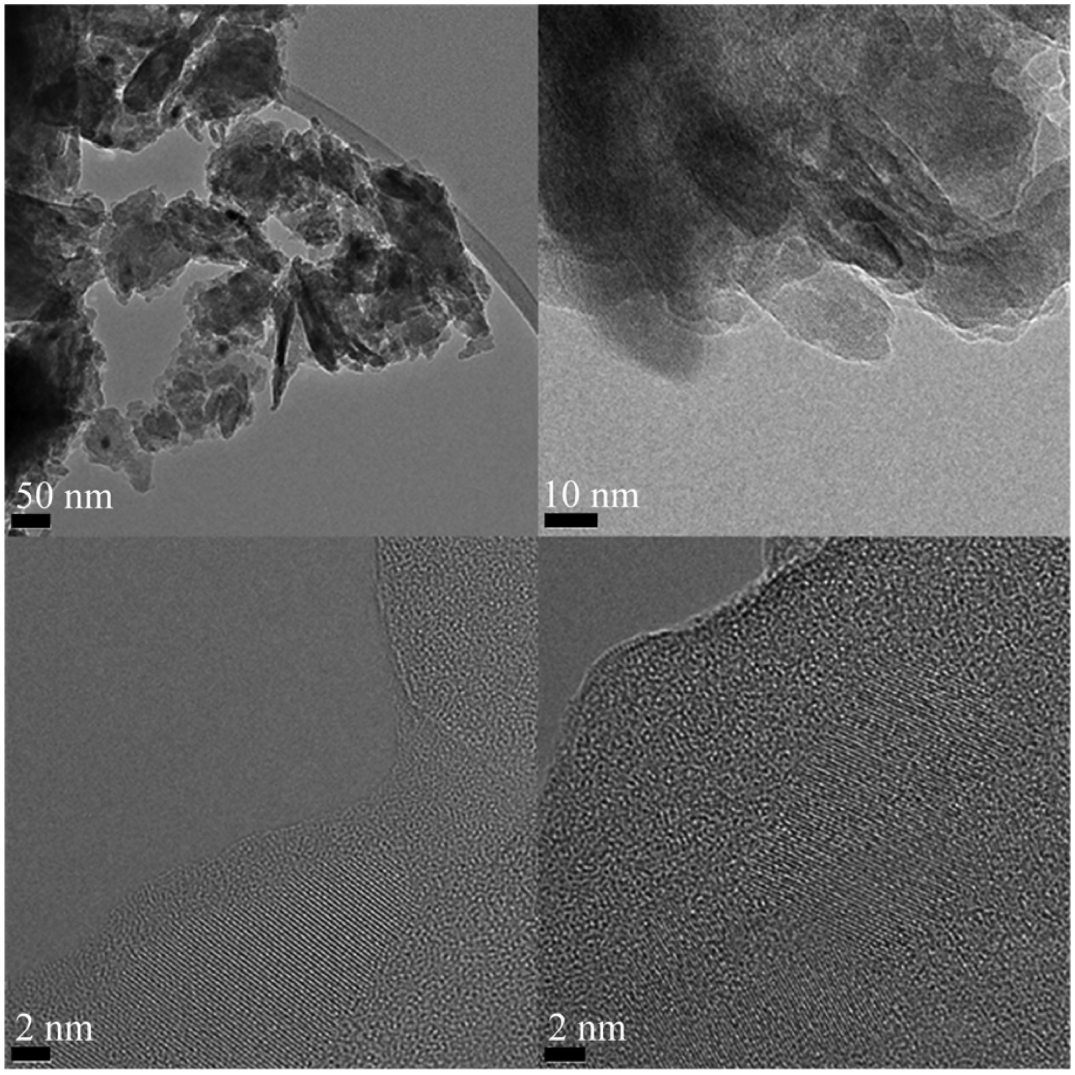

Figure 3. TEM images showing size distribution and crystal structure of boron-coated aluminum nanoparticles. (Diborane−Al nanoparticles remilled in diborane with WC balls.)

of 0.18) As shown below, however, the actual B/Al mole ratio was substantially higher, again consistent with the fills having a significant amount of liquid pentaborane.

4.1.3. Reactivity of Diborane- and Pentaborane-Milled Aluminum Particles. The particles produced with the two boranes were chemically quite different, as shown by their behavior when exposed to air. Small samples of both the diborane- and pentaborane-milled materials were exposed in the glovebox to allow any residual boranes to evaporate and then sealed in small screw-top glass vials. The vials were brought out of the glovebox into a fume hood, uncapped, and poured out. The most pyrophoric particles we had previously produced were generated by milling Al balls in acetonitrile vapor, leaving a thin surface layer with an $Al_nC_mN_oH_p$ composition.[16] Those particles ignited as they were poured out of the vial and burned vigorously enough to be completely consumed as they fell a few centimeters. Particles produced by milling Al balls in diborane were also found to be pyrophoric, but ignition and combustion were comparatively slow, suggesting that the surface layer was less reactive. In fact, the ignition and combustion behavior was visually similar to that for unpassivated boron nanoparticles in a similar size range.[32] In contrast, the sample produced by milling in pentaborane deflagrated violently enough to crack the sample vial as the cap was removed. Given that pentaborane itself reacts explosively with air, it is possible that the violent reaction resulted from residual pentaborane vapor, despite our having allowed ∼30 min for residual pentaborane (200 Torr vapor pressure) to evaporate in the glovebox. Alternatively, it is possible that a layer of pentaborane might have remained chemisorbed on the surface or that the surface itself had borane-like B−H functionalization.

In addition to high reactivity with air, pentaborane-milled aluminum was found to ignite, sometimes violently, upon contact with ethanol, acetonitrile, and some ionic liquid (IL) materials, even under s N_2 atmosphere. These materials had all been degassed by freeze−pump−thaw cycles (ethanol, acetonitrile) or by prolonged evacuation (ILs) in the glovebox load-lock chamber and were all compatible with aluminum powder produced by milling in acetonitrile or diborane vapors.

4.1.4. Particle Size and Morphology. Particle size and morphology were assessed by a combination of DLS and electron microscopy. To perform DLS experiments safely on particles without a hydrocarbon capping layer, diborane-milled particles were first suspended in degassed hexanes in a nitrogen-filled glovebox, and then the suspension was exposed

DOI: 10.1021/acs.jpcc.7b03583
J. Phys. Chem. C 2017, 121, 14176−14190

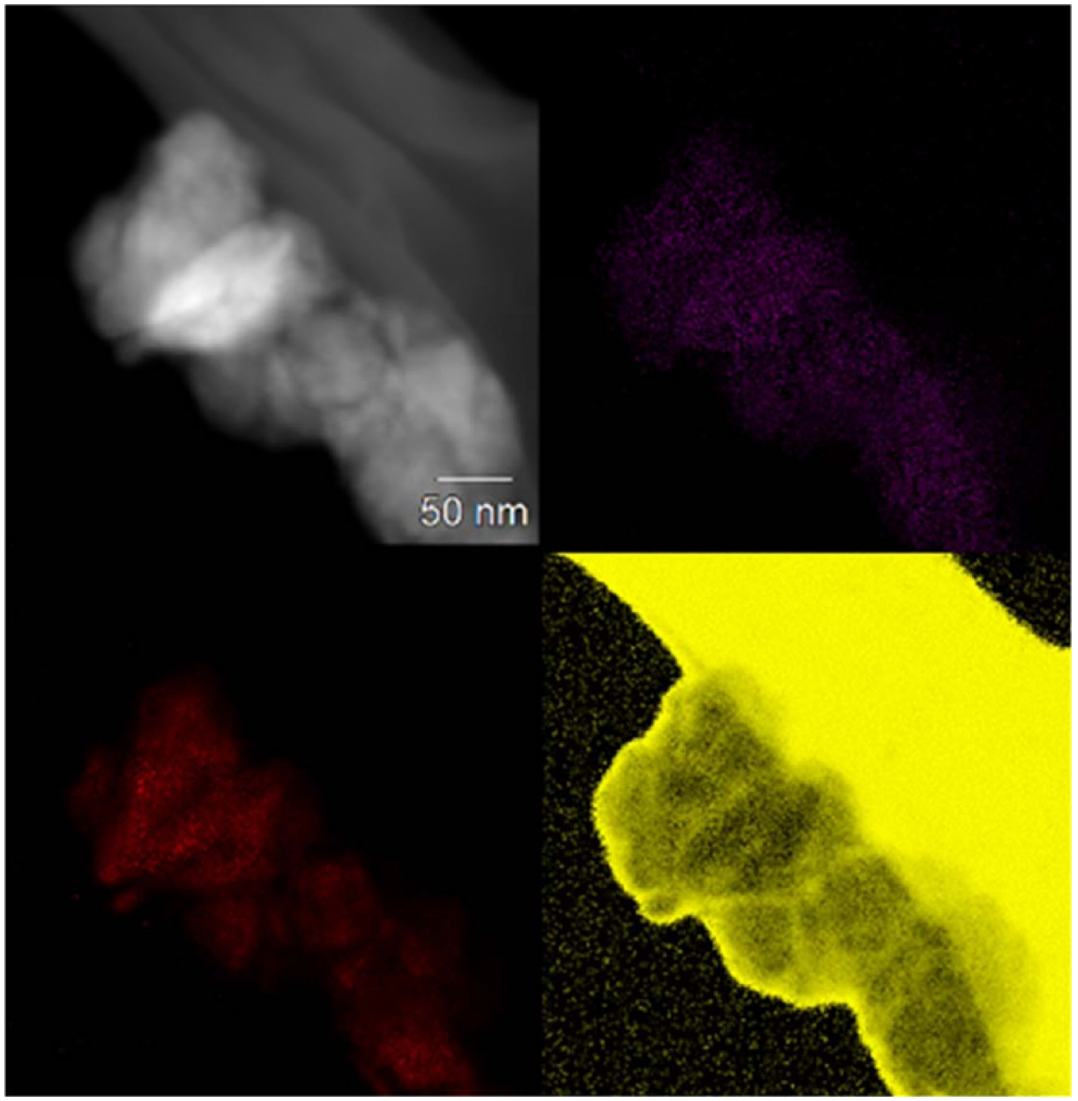

Figure 4. (Top left) STEM image of pentaborane-milled aluminum capped with 1-octene at 300 rpm and EDS mappings of (top right) boron, (bottom left) aluminum, and (bottom right) carbon.

to air in a fume hood overnight. O_2 has solubility in *n*-hexane of only ~2 mM,[33] and the idea was to passivate the particles by slow oxygen diffusion through the hexanes, with minimal modification or aggregation. Particles passivated in this way were modestly dispersible in hexanes, with a significant fraction precipitating out of suspension during the ~10-min DLS acquisition time. This approach was not attempted for the more reactive pentaborane-milled particles, for fear that they would ignite the hexanes.

To passivate the particles and improve their dispersibility for DLS analysis, the particles were capped with ligands, as described above. Oleic acid (OA) binds well to both boron[32] and aluminum[14] nanoparticles and was found to impart reasonable dispersibility to the diborane-milled particles. Alkenes react with B−H-terminated boron nanoparticle surfaces,[18] and because mass spectrometry suggested (Figure 1) that the borane-milled aluminum particles had both B and H in the surface layer, we also tried capping the particles by milling a sample of diborane-milled particles with 1-octene, using WC balls and a milling speed of either 100 or 300 rpm. Particles milled at 100 rpm with octene were actually less hexanes-dispersible than uncapped particles, forming clumps within 1 min; however, the sample produced by milling with octene at 300 rpm was highly dispersible in hexanes.

Typical DLS results are summarized in Figure 2. The left side shows results for particles produced by milling Al balls in diborane, milling them again in diborane using WC balls, and then passivating them by slow air exposure in hexanes. The right side shows results for particles produced by milling Al balls in diborane and then milling them again with 1-octene using WC balls at 300 rpm for passivation. Each sample was ultrasonicated briefly just before analysis to resuspend any sediment, and then the DLS size distribution in panel A was taken with a 10-min acquisition time. The distributions in panels B−D were taken sequentially with 10-min acquisition times, so that panels A−D follow the particle size distributions for ~40 min after the initial ultrasonication of the particles prior to DLS. For the uncapped particles produced with diborane, the initial DLS distribution (panel A, left) shows two size modes, with over half the particle mass in the 30−50-nm size range, but with a substantial mode centered at about 1 μm. The three subsequent DLS experiments show that the nanoparticle size mode gradually shifted to larger size and weakened with time, whereas the micrometer size mode strengthened and

DOI: 10.1021/acs.jpcc.7b03583
J. Phys. Chem. C 2017, 121, 14176−14190

shifted to larger size. Given that these particles were found to be only modestly dispersible in hexanes, the obvious interpretation is that the primary particles were mostly in the 30−50-nm range, but that they formed micrometer-scale aggregates that grew with time.

The octene-capped particles showed qualitatively similar results, with a 30−50-nm size mode that shifted to larger size and weakened over time and a 2−3-μm size mode that grew and shifted to larger size. Curiously, even though the octene-capped particles were far more hexanes-dispersible than the uncapped particles, the size distribution was dominated by the micrometer-scale aggregates, even during the initial DLS experiment. DLS measures the size distribution for particles that remain in suspension on the ∼10-min measurement time scale. For the uncapped particles, which precipitated out of the suspension on a ∼10-min time scale, DLS detected mostly the nanoparticles along with the fraction of the micrometer-scale aggregates that remained in suspension. For the octene-capped particles, aggregation of the primary nanoparticles into micrometer-size aggregates also occurred, but the aggregates tended to remain in suspension and, therefore, to dominate the light scattering. In both cases, DLS suggests that the primary particles had hydrodynamic radii in the 30−50-nm range.

Figure 3 shows several transmission electron microscopy (TEM) images for uncapped particles made by milling Al balls in diborane, remilling the particles in diborane with WC balls, passivating them in hexanes (i.e., the same particles as in the left column of Figure 2), and drop-casting them onto a lacey carbon TEM grid. The images in Figure 3 were taken on a probe-corrected S/TEM instrument at Argonne National Laboratory, but because of the low contrast for boron and aluminum, detailed imaging was difficult. The particles clearly aggregated during drying, and the primary particles had lateral dimensions in the 50−200-nm range, but appeared to have a flattened, flake-like morphology, which might explain why they appeared smaller in DLS measurements. Aluminum nanoparticles produced by milling Al balls in acetonitrile vapor (without remilling with WC balls) also appeared to have a flake-like morphology, as shown by He ion microscopy,[16] suggesting that attrition from Al balls tends to produce this shape. In the higher-magnification images, lattice fringes can be seen in nanocrystalline regions in the cores of the particles, and electron diffraction (Figure S7) was consistent with the cores being fcc aluminum. The high-magnification images also indicate an amorphous layer 2−5 nm thick on the surface of the particles.

We also used the Utah S/TEM instrument, which is not probe-corrected but does have dual-detector energy-dispersive X-ray spectroscopy (EDS) capability, to image and perform elemental mapping of a small aggregate of particles adhering to a strand of lacey carbon on a TEM grid, as shown in Figure 4. This sample was produced by milling in pentaborane and then capping the particles with 1-octene by milling with WC balls at 300 rpm. In the TEM image at the upper left, contrast is low, but the primary particles appear to have had lateral dimensions in the 50−150-nm range.

4.1.5. XPS, EELS, and EDS Studies of Particle Composition and Structure. To probe the distributions and oxidation states of elements in the particles, a combination of X-ray photoelectron spectroscopy (XPS), electron-energy-loss spectroscopy (EELS), and EDS was used, the latter two in conjunction with S/TEM. EELS was performed at Argonne National Laboratory on the same sample that was imaged in Figure 3, namely, particles prepared by milling Al balls in diborane, remilling the particles in diborane with WC balls, and then stabilizing them by slow oxidation. EELS was used to study the edge of one particle shown in Figure 3, and the spectrum (Figure S6) shows a large aluminum signal at ∼70 eV and a weak feature from boron near 190 eV, as expected given the low boron concentration in the sample. The boron peak was considered to be too weak for quantitation.

EDS elemental mapping was done with the Utah S/TEM instrument on pentaborane-milled, octene-capped particles, and Figure 4 shows maps for aluminum, boron, oxygen, and carbon. The carbon signal is highest at the edges of the particles, indicating that it mostly originates from the particle surfaces, as expected for 1-octene-capped material. Conversely, the Al signal is strongest in the highest-contrast (thickest) regions, as expected for Al in the particle cores. The boron signal is too weak to allow resolution of this type of structural detail; however, it is clear that the B/Al stoichiometry is quite uniform across the ensemble of particles, as opposed to distinct Al-rich and B-rich particles.

Although the boron EDS signal was weak, by averaging over the particles, we found the B/Al mole ratio to be ∼0.37, or ∼0.61 after correction for self-absorption using the Cliff−Lorimer method, assuming the sample thickness to be 50 nm.[34] Note that B Kα line was weak and fell on the shoulder of the large carbon Kα line originating from the octene coating and carbon support; thus, both counting statistics and background subtraction by the EDS software resulted in a large uncertainty in the boron concentration. For what it is worth, however, the B/Al ratio from EDS was substantially larger than the ratio (0.18) that would be estimated from the milling stoichiometry, if we assumed that only saturated pentaborane vapor was present in the mill jar. Therefore, EDS also supports the aspiration of a significant amount of liquid pentaborane into the jar.

XPS was used to obtain additional insight into the distribution of boron within the particles, as well as the oxidation states of both boron and aluminum. Figures 5 and 6 present Al 2p and B 1s spectra for a variety of borane-milled aluminum samples. Table 1 reports the integrated B 1s and Al 2p intensities for all six samples studied, along with two B/Al intensity ratios for each. The first is simply the ratio of raw integrated intensities, and the second is scaled by the

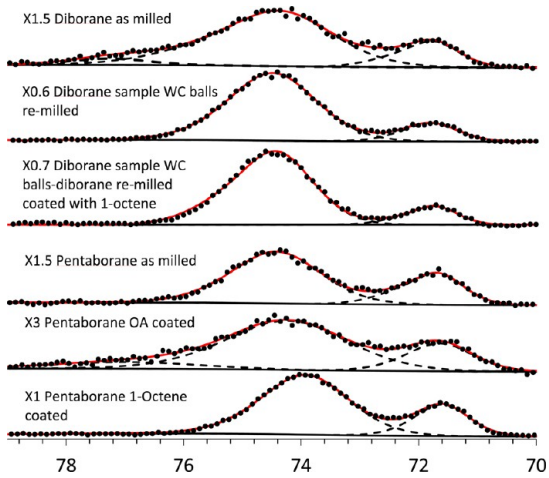

Figure 5. High-resolution XPS spectra of the Al 2p.

DOI: 10.1021/acs.jpcc.7b03583
J. Phys. Chem. C 2017, 121, 14176−14190

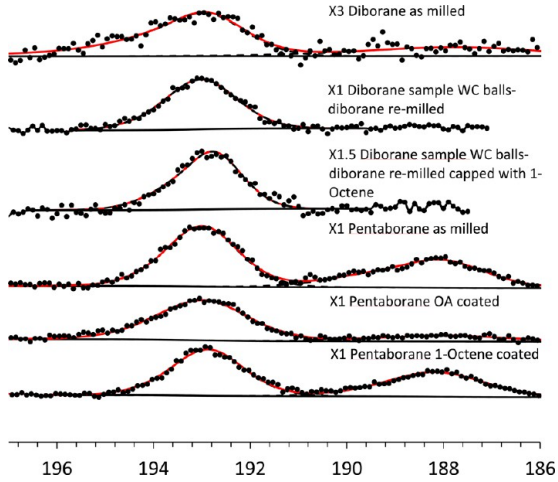

Figure 6. High-resolution XPS spectra of the B 1s region.

Table 1. Boron/Aluminum Ratios Calculated from XPS Data

	integrated area from XPS		B/Al ratio	
	B	Al	without ASF correction	with ASF correction
		B_2H_6		
as-milled	1163.7	4955.1	0.23	0.29
1-octene-capped	2315.6	8784.9	0.26	0.32
WC-remilled	2811.1	10470.7	0.27	0.33
		B_5H_9		
as-milled	5645.8	4038.2	1.39	1.70
1-octene-capped	3225.2	6328.2	0.51	0.62
WC-remilled	4431.0	2529.6	1.75	2.13

tabulated[35] atomic sensitivity factors (ASFs) for B 1s and Al 2p. The ASF-corrected ratios would give the B/Al stoichiometry if the samples were homogeneous. Consider the diborane-milled samples, where the total amount of boron present is well-known from the milling stoichiometry (7 mol % for particles as-produced or 1-octene-capped; 11 mol % for particles remilled with WC balls in diborane, labeled "WC-remilled"). The ASF-corrected XPS B/Al ratios are 3−4 times higher than the experimentally determined B/Al stoichiometries, implying that boron must have been concentrated in the surface layer of the particles, where it was detected by XPS with enhanced sensitivity. XPS sensitivity varies with depth as exp(−depth/EAL), where "depth" refers to the distance below the surface along the photoelectron detection direction and EAL is the electron effective attenuation length. Over 85% of the XPS signal originates within 2(EAL) of the surface, and the high B/Al XPS ratios imply that a substantial fraction of the boron must have been in this near-surface layer. The inference of a boron-rich surface layer is not surprising, given that the particles were produced by attrition of aluminum particles into diborane, which reacts with the aluminum surface, as shown above.

XPS was also used to obtain information regarding the oxidation states of both B and Al. For diborane-milled samples, the boron was essentially all oxidized, generating a peak near the 193 eV binding energy expected for B^{3+}, with essentially no signal at about 188 eV, where B^0 is observed.[35] This oxidation must have occurred when the samples were transferred in air to the XPS spectrometer, and similar levels of oxidation would have occurred in the TEM samples. Some signal was observed for unoxidized boron for the pentaborane-milled particles, both for particles that were passivated by slow oxidation and for particles capped with 1-octene. In contrast, pentaborane-milled particles capped with oleic acid (OA) showed little B^0 signal at about 188 eV. It is not clear why there should be unoxidized boron in these particles, although it might simply mean that the boron-rich surface layer was thick enough that it only partially oxidized upon air exposure.

For all samples, the Al 2p spectra show two peaks. The larger peaks appearing at 74−74.5 eV in the spectra are in the 73.6−74.7 eV binding energy range typically reported for Al^{3+} in Al_2O_3[36−39] and are therefore assigned to oxidized aluminum in the surface layer. The low-binding-energy peaks at ∼71.6 eV are assigned to Al^0 in the particle cores, even though this binding energy is slightly below the range typically reported for bulk aluminum (72.0−72.9 eV).[39−44]

To obtain more quantitative insight into the particle structure, it is useful to model the XPS spectra using electron effective attenuation lengths (EALs) obtained using the NIST EAL program of Powell and Jablonski.[45] The model is based on following observations: TEM shows metallic (fcc) aluminum cores, capped with an amorphous layer a few nanometers thick. XPS shows that the surface layer of the air-transferred particles is oxidized. As shown below, the B/Al XPS ratio implies that this surface layer is boron-rich, and headspace mass spectrometry implies that the samples retained significant hydrogen, presumably also in the surface layer. Therefore, the model is of metallic Al particles with an oxidized surface layer of $Al_nB_oH_pO_x$ stoichiometry. The EALs in the oxidized layer were calculated based on B/H/Al ratios determined from the milling stoichiometry and assuming the presence of enough oxygen (from air exposure) to fully oxidize the layer. Fortunately, EALs are weakly dependent on composition, so the assumed $Al_nB_oH_pO_x$ stoichiometry is not critical in the modeling. Furthermore, the B 1s and Al 2p photoelectrons have similar kinetic energies (∼1300 and ∼1410 eV, respectively) and thus have similar EALs. The estimated EALs are 2.3 and 2.7 nm for Al 2p electrons passing through the aluminum core and the $Al_nB_oH_pO_x$ surface layer, respectively. The EAL for B 1s photoelectrons within the $Al_nB_oH_pO_x$ layer is 2.5 nm. For ligand-capped particles, the EALs in the hydrocarbon capping layer are estimated to be 3.4 and 3.7 nm for B 1s and Al 2p electrons, respectively.

For bulk aluminum capped with an oxidized $Al_nB_oH_pO_x$ layer, we used the Al^{3+}/Al^0 XPS intensity ratio to estimate the thickness of the oxidized layer and the B/Al intensity ratio to provide insight into the distribution of boron in the samples. We tested three different models, focusing on the simplest sample: particles produced by milling in diborane and then passivated without addition of a hydrocarbon capping layer. For this sample, the B/Al ratio was well determined from the milling stoichiometry. The first model treated the sample as planar bulk aluminum covered by a homogeneous $Al_nB_oH_pO_x$ layer. The thickness of the oxide layer was allowed to vary, with the total boron content held constant at ∼38 atoms/nm^2, as determined from the milling stoichiometry (see above). To fit the measured Al^{3+}/Al^0 ratio, the thickness of the oxidized layer needs to be ∼3 nm; however, for a homogeneous $Al_nB_oH_pO_x$ layer of this thickness, the calculated B/Al XPS ratio is only ∼7%, compared to 23% measured for the passivated particles (Table 1). Evidently, boron was concentrated near the surface, where it was detected with higher efficiency.

DOI: 10.1021/acs.jpcc.7b03583
J. Phys. Chem. C 2017, 121, 14176−14190

Our second model also assumed a planar sample, but with three layers: a bulk elemental aluminum base layer, capped with a thin layer of aluminum oxide, and an outer layer of boron oxide. Because this model puts the boron in the topmost layer, where XPS sensitivity is highest, it does lead to an increase in the calculated B/Al XPS ratio to ∼12%—still significantly lower than the measured ratio.

Of course, the particles are not planar, but rather a jumbled mass of irregular particles with random orientations. For simplicity, we modeled this situation as a collection of ∼50-nm spherical particles.[46] Such particles are large enough compared to the EALs that it is necessary to consider only electrons generated near the surface of the top half of each particle. For electrons generated near the tops of the spheres, where the detection direction is normal to the surface, the intensity ratio is identical to that for a planar model. As the emission position moves away from the top, however, the path length along the detection direction becomes greater, which increases XPS sensitivity to the surface layer, relative to the bulk, thereby enhancing both the B and Al^{3+} sensitivities. To fit the Al^{3+}/Al^0 XPS ratio, the total thickness of the oxidized layer decreases to ∼2 nm, giving a B/Al XPS ratio of 17%. The fact that this model result is still somewhat lower than the observed ratio (23%) is not surprising. The particles are actually rough, and any nanoscale asperities will tend to enhance the contribution of the surface layer to the XPS spectrum. We conclude that the particles were coated with an oxidized layer on the order of ∼2 nm thick, with boron concentrated near the surface. For reference, planar bulk boron surfaces form a native oxide layer upon air exposure that is ∼0.4 nm thick, small enough compared to the EAL that B^0 is easily seen through the oxide layer in XPS.[47] For pure bulk aluminum, the thickness of the native oxide layer is ∼3−4 nm,[13] and for some aluminum alloys, it can be up to 10−15 nm thick.[48] Therefore, we can conclude that boron in the surface layer does provide modest protection to the aluminum particle cores, but that the extent of oxidation is still much greater than for pure boron.

Based on this XPS estimate of a 2-nm-thick oxidized layer on 50-nm-equivalent-diameter particles, we estimate that the volumetric energy release that would result from oxidizing the particles would be ∼73.8 MJ/L, corresponding to ∼88% of the theoretical energy release from pure unoxidized aluminum combustion.

For the diborane-milled samples, the raw B/Al XPS intensity ratio is 0.23 for particles as-prepared by milling Al balls, increasing to 0.27 for the particles remilled with WC balls in diborane. The stoichiometries calculated from the diborane fills are 7 and 11 mol %, that is, remilling adds ∼50% more boron, whereas the increase as measured by XPS is only ∼20%. Milling of ductile materials such as aluminum[14] is expected to result in significant working and cold welding of nascent boron-coated particles, which would tend to mix boron deeper into the particles or to trap boron in buried interfaces between aggregated particles, in either case reducing the XPS-accessible fraction. It is not clear, however, why WC milling with 1-octene to add a hydrocarbon capping layer also leads to an increase in the B/Al ratio to 0.26, even though no additional diborane was used. B/Al XPS ratios up to 8 times higher were observed for the pentaborane-milled samples, compared to the diborane-milled materials, providing further evidence that there must have been significant liquid pentaborane present in the jar fills, increasing the boron concentration and/or the thickness of the boron-rich surface layer. The substantially lower ratio for the octene-capped pentaborane-milled sample is probably due to the way this sample was prepared. 1-Octene was mix-milled with a sample of particles and WC balls, and then the resulting hexanes-dispersible particles were repeatedly centrifuged out of suspension and resuspended in fresh hexanes to remove excess 1-octene. Some small particles could not be centrifuged out, and these might have carried away some of the boron-rich surface layer of the as-prepared particles.

We showed that, for B−H-terminated boron nanoparticles produced by milling boron powder in H_2, air oxidation can be prevented by capping the particles with alkenes such as 1-octene.[18] For borane-milled aluminum particles, the enhanced hydrocarbon dispersibility after mix milling with 1-octene indicates that the surface does become hydrocarbon-capped; however, the alkyl layer clearly has little effect on surface oxidation. After air exposure, the boron is entirely oxidized, and the Al^{3+}/Al^0 ratio is quite similar to that for particles without the organic ligands. The estimated thickness of the oxidized layer is still ∼2 nm, and from the C/Al ratio, we estimate that the organic capping layer was 1−2 nm thick, including any adventitious carbon on the surface.[49] To compare the effectiveness of different ligands, pentaborane-milled particles were capped with both oleic acid (OA) and 1-octene, and their XPS spectra are compared to those of uncapped, passivated particles in Figures 5 and 6. The aluminum spectra of all samples are similar, with a large Al^{3+} peak at ∼74.5 eV and a smaller Al^0 peak at ∼72 eV. Again, this similarity tends to suggest that the ligand coatings have little protective effect on the aluminum surface, as Chung et al. observed for alkyl-substituted epoxide-capped aluminum nanoparticles.[50] There was, however, a significant reduction in the B^0/B^{3+} ratio for the OA-capped particles, presumably due to formation of B−O bonds during interactions with the carboxylate group on OA.

As an initial probe of the oxidation properties of the ligand-capped particles, a sample of pentaborane-milled, oleic acid-capped particles was first exposed to air for several hours and then shipped under N_2 to Johns Hopkins University. The sample was introduced into a surface analysis instrument, and the Al 2p and B 1s XPS spectra were recorded. The sample was then heated to 300 °C to destabilize the ligand layer, re-examined by XPS, then exposed to 1×10^{-5} Torr of oxygen at 300 °C, and examined again by XPS. The results, summarized in Figures S8 and S9, show two main effects. Both the B 1s and Al 2p peak intensities increased substantially after 300 °C heating, indicating decomposition/desorption of a significant fraction of the ligand layer, resulting in less attenuation of the signals from underlying boron and aluminum. The intensities increased further after O_2 exposure, suggesting that oxidation removed additional ligand material. There were also changes in the oxidation state of both elements. The Al^{3+}/Al^0 ratio changed from ∼3.9:1 to ∼12:1 after heating and to ∼19:1 after O_2 exposure. The B^{3+}/B^0 ratio changed from ∼5.5:1 to 10:1 after heating, with no further change after O_2 exposure. The increase in oxidation state after heating in a vacuum is attributed to some combination of reaction with the $\sim 10^{-8}$ Torr of H_2O in the chamber background and reaction with O atoms in the ligand carboxylate groups as the ligand layer decomposed and desorbed. Regardless of the source, it is clear that the ligand layer at least partially protected the underlying boron and aluminum from air oxidation.

4.2. Theoretical Results. *4.2.1. Chemisorption of B_2H_6.* In the following discussion, all energies given in the text are ZPVE-corrected, unless otherwise noted, and both the

DOI: 10.1021/acs.jpcc.7b03583
J. Phys. Chem. C 2017, 121, 14176−14190

electronic and ZPVE-corrected values are generally given in the figures. DFT calculations of a single diborane molecule interacting with various sites on the Al_{80} cluster revealed that B_2H_6 weakly binds to the cluster surface by physisorption (henceforth denoted as B_2H_6:Al_{80}) or chemisorption (denoted as B_2H_6–Al_{80}), as shown in Figures S10 and S11, respectively. Physisorption, defined here as preserving the diborane reactant bonding, has binding energies ranging from −3 to −5 kcal mol^{-1} relative to separated diborane and Al_{80}. In the chemisorbed structures, one or more bonds in diborane are broken, and the binding ranges from being slightly endothermic (+2 kcal mol^{-1}) to being exothermic by 8 kcal mol^{-1} (Figure S11.) The variation in binding energies is due in part to the multiple binding motifs of boron and hydrogen to the cluster surface; that is, both boron and hydrogen can form bridging or terminal bonds to the cluster surface. Another contributing factor is the local heterogeneous structure (i.e., "roughness") of the Al_{80} cluster surface, which is likely similar to the surfaces formed by fracturing in the ball-milling process. Conversion of physisorbed B_2H_6 to a chemisorbed species is predicted to cross a barrier of only 11−12 kcal mol^{-1}, as seen in the two computed reaction pathways shown in Figures S12 and S13. The barrier for the reverse process is similarly modest (7 kcal mol^{-1}), indicating that interconversion between physisorbed and chemisorbed species should readily occur under the ball-milling conditions, where instantaneous local temperatures during ball collisions can reach >1000 K.[51]

4.2.2. Fragmentation of B_2H_6. One possible means for chemisorbed diborane to fragment on the aluminum surface is by B−H bond scission to form chemisorbed B_2H_5 and H fragments, that is, B_2H_6–Al_{80} → B_2H_5–Al_{80}–H. Relative to separated Al_{80} + B_2H_6, the enthalpies of chemisorbed B_2H_5 and H range from +6 to −13 kcal mol^{-1}, as illustrated in Figure S14. The local minima shown in Figure S14 reveal that B_2H_5 can bind to the Al_{80} surface through monodentate or bidentate configurations, where the former is less stable than the latter. A saddle point connecting chemisorbed diborane and bidentate B_2H_5 and H fragments was located and is shown in Figure S15. The barrier of 13 kcal mol^{-1} for this pathway should be easily traversed under ball-milling conditions. A similar saddle point leading to the formation of monodentate chemisorbed B_2H_5 and H was also located and is shown in Figure S16, with a higher barrier of 20 kcal mol^{-1}. In addition, a saddle point connecting physisorbed diborane with chemisorbed B_2H_5 and H (B_2H_6:Al_{80} → B_2H_5–Al_{80}–H) was located, with a corresponding barrier of 30 kcal mol^{-1}, as illustrated in Figure S17.

Chemisorbed B_2H_5 can undergo a second B−H fragmentation step, namely, B_2H_5–Al_{80}–H → B_2H_4–Al_{80}–2H. As displayed in Figure S16, the relative enthalpies of B_2H_4–Al_{80}–2H range from 0 to −11 kcal mol^{-1}. (Note that B_2H_4–Al_{80}–2H is more stable than chemisorbed B_2H_4 + gaseous H_2, as shown by comparing Figures S18 and S19.) A saddle point for the second B−H fragmentation was located and is shown in Figure S20. The barrier is 18 kcal mol^{-1}, which is 5 kcal mol^{-1} larger than the barrier for the initial B−H fragmentation step (see Figure S15.) Subsequent B−H fragmentations leading to the formation of chemisorbed B_2H_3, B_2H_2, B_2H, and B_2 were not considered.

A second fragmentation pathway of chemisorbed diborane is cleavage of the B−B bond to form two chemisorbed BH_3 fragments, that is, B_2H_6–Al_{80} → H_3B–Al_{80}–BH_3. Relative to separated Al_{80} + B_2H_6, the enthalpies of H_3B–Al_{80}–BH_3 range from −5 to −23 kcal mol^{-1}, as shown in Figure S21. Therefore, H_3B–Al_{80}–BH_3 is more stable on average than chemisorbed diborane B_2H_6–Al_{80}, which has binding energies ranging from +2 to −8 kcal mol^{-1}, indicating that B−B fragmentation is an energetically favorable process. Likewise, H_3B–Al_{80}–BH_3 is more stable on average than B_2H_5–Al_{80}–H (with binding energies ranging from +6 to −13 kcal mol^{-1}), indicating that B−B fragmentation leads to more stable products than B−H scission. As shown in Figure S20, the barrier for B−B dissociation is 18 kcal mol^{-1}, slightly larger than the barrier of 13 kcal mol^{-1} for B−H fragmentation (Figure S15) but still readily accessible under ball-milling conditions. Therefore, it is plausible that both B−B and B−H fragmentation readily occur on the aluminum surface.

4.2.3. Formation of H_2. H_2 is the primary gaseous byproduct of Al milling in the presence of diborane (Figure 1), although it is clear that much of the hydrogen in diborane is retained in the surface layer. Several possible reactions leading to the formation of H_2 were investigated. One possible route to the formation of H_2 is through direct elimination from chemisorbed B_2H_6, namely, B_2H_6–Al_{80} → B_2H_4–Al_{80} + H_2, as illustrated by the reaction pathway shown in Figure S23. The electronic-only surface (i.e., excluding ZPE corrections) shows a two-step process proceeding through two transition states connected by a metastable reactive intermediate in which the departing H_2 is weakly complexed to one of the boron atoms. However, upon inclusion of ZPE corrections, the second transition state becomes lower in energy than the metastable intermediate, indicating that H_2 elimination is actually a single-step process, with an endothermic reaction enthalpy of +4 kcal mol^{-1} and a barrier of only 16 kcal mol^{-1}. An energetically less favorable pathway for unimolecular elimination of H_2 from chemisorbed diborane, with a barrier and reaction enthalpy of +30 and +29 kcal mol^{-1}, respectively, resulting in the formation of chemisorbed $BHBH_3$ (B_2H_6–Al_{80} → $BHBH_3$–Al_{80} + H_2), was located and is shown in Figure S24.

A second unimolecular H_2 elimination mechanism, B_2H_4–Al_{80} → B_2H_2–Al_{80} + H_2, was investigated. Two distinct reaction pathways were found for this process, as shown in Figures S25 and S26. This mechanism is considerably less favorable than the direct H_2 elimination from diborane illustrated in Figure S23, in terms of both reaction endothermicities (+23 vs +20 kcal mol^{-1}) and barriers (38 vs 35 kcal mol^{-1}). Unimolecular H_2 elimination from chemisorbed BH_3, with a second chemisorbed "spectator" BH_3 fragment, was also considered and found to have a large barrier of 41 kcal mol^{-1}, as shown in Figure S27.

There are many possible "bimolecular" routes to H_2 formation involving the elimination of H_2 from neighboring chemisorbed fragments. In the above discussion of diborane decomposition, it was shown that B−B and B−H bond fragmentations are energetically accessible, suggesting the possible presence of H, B_2H_5, B_2H_4, BH_3, and perhaps smaller B_2H_x and BH_x species as well, chemisorbed on the aluminum surface along with the parent B_2H_6. In principle, H_2 could be generated by bimolecular elimination from any pair of these fragments. Although a comprehensive investigation of all possible bimolecular H_2 elimination pathways is beyond the scope of the present study, a subset of these routes was mapped out. One of these is the reaction B_2H_6–Al_{80}–2H → B_2H_5–Al_{80}–H + H_2, shown in Figure S28, where a second spectator chemisorbed H atom was included to preserve a closed-shell electronic state for consistency. This pathway encounters a barrier of 30 kcal mol^{-1} and is endothermic by 2 kcal mol^{-1}. As

DOI: 10.1021/acs.jpcc.7b03583
J. Phys. Chem. C 2017, 121, 14176−14190

shown in Figure S29, the reaction B_2H_5–Al_{80}–H → B_2H_4–Al_{80} + H_2 crosses a barrier of 32 kcal mol^{-1} but is exothermic by 5 kcal mol^{-1}. The bimolecular elimination reaction B_2H_4–Al_{80}–2H → B_2H_3–Al_{80}–H + H_2 (see Figure S30) has a larger barrier of 38 kcal mol^{-1}, as well as a larger reaction endothermicity of +16 kcal mol^{-1}. Finally, three saddle points (not shown) with barriers ranging from 41 to 44 kcal mol^{-1} for the formation of H_2 through the reaction BH_3–Al_{80}–2H → BH_2–Al_{80}–H + H_2 (which has not been confirmed by IRC calculations) were located. Several additional bimolecular elimination pathways were investigated but found to have significantly larger barriers than the pathways cited above, such as the formation of H_2 from H_3B–Al–BH_3, as shown in Figure S31. These are not discussed further. Finally, as shown in a previous study,[14] recombination of H atoms adsorbed on Al_{80} to form H_2 has a barrier of 25 kcal mol^{-1} and is endothermic by 4 kcal mol^{-1}. A summary of the computed barriers and reaction enthalpies for all of the pathways leading to formation of H_2 is provided in Table 2. The data in Table 2 show that unimolecular elimination of H_2 from chemisorbed diborane has the smallest energy barrier (16 kcal mol^{-1}) of all of the H_2-producing reactions considered.

Table 2. M06/6-311++G(d,p) Barriers and Enthalpies of Reaction (kcal mol^{-1}) for the Generation of H_2

reactant(s)	$\Delta H^{\ddagger}$	ΔH_{rxn}
	Unimolecular	
B_2H_6–Al_{80}	15.9	3.6
	29.7	28.7
B_2H_4–Al_{80}	38.4	23.0
	35.4	19.8
BH_3–Al_{80}	40.7	9.6
	Bimolecular	
B_2H_6–Al_{80}–H	29.9	1.8
B_2H_5–Al_{80}–H	31.5	−4.7
B_2H_4–Al_{80}–H	37.6	7.2
BH_3–Al_{80}–BH_3	59.4	20.2
	61.7[a]	22.1[a]
BH_3–Al_{80}–H	41.0[a]	15.4[a]
	43.6[a]	15.4[a]
	44.3[a]	15.4[a]
B_2H_6–Al_{80}–B_2H_6	33.4[a]	−11.7[a]
B_2H_5–Al_{80}–B_2H_5	63.3[a]	n/a
H–Al_{80}–H	25[b]	4[b]

[a]Not confirmed by IRC calculations. [b]From ref 14.

In summary, the kinetically most favorable route to the generation of H_2 in the milling of Al with diborane involves two steps: (1) chemisorption of diborane, which crosses a barrier of 11–12 kcal mol^{-1} (Figures S12 and S13), followed by (2) unimolecular elimination of H_2, which has a barrier of 16 kcal mol^{-1} (Figure S23). Additional pathways that should be readily accessible under the ball-milling conditions include B–H fragmentation (barrier of 13 kcal mol^{-1}; Figure S15) and B–B fragmentation (barrier of 18 kcal mol^{-1}; Figure S22). In general, diborane is predicted to be highly reactive with aluminum under milling conditions, consistent with the rapid consumption observed.

4.2.4. Chemisorption of B_5H_9. Similarly to diborane, pentaborane interacts weakly with the aluminum surface by either physisorption or chemisorption, as displayed in Figures S32 and S33, respectively. For physisorbed pentaborane, the binding energy ranges from −5 to −7 kcal mol^{-1}. The relative energies of chemisorbed pentaborane range from slightly endothermic (+4 kcal mol^{-1}) to exothermic by 14 kcal mol^{-1}. Conversion of physisorbed B_5H_9 to a chemisorbed form crosses a barrier of 29 kcal mol^{-1}, as shown in Figure S34. It is important to note that this barrier is significantly larger than the 11–12 kcal mol^{-1} barrier for the chemisorption of diborane (Figures S12 and S13), indicating that pentaborane is more resistant to chemisorption than diborane. This is consistent with the lower rate of consumption of pentaborane observed in the milling experiments.

4.2.5. Fragmentation of B_5H_9. Because B–B fragmentation of chemisorbed pentaborane is likely to be a complex, multistep process, it is not considered here. In regard to B–H fragmentation, several possible B_5H_8–Al_{80}–H conformers of the products of B–H bond dissociation in chemisorbed pentaborane are shown in Figure S35 and range in energy from +2 to −16 kcal mol^{-1}, relative to separated B_5H_9 + Al_{80}. Two reaction pathways for this process are shown in Figures S36 and S37. In the former (latter), the barrier and reaction enthalpy are 16 (36) and −16 (+3) kcal mol^{-1}, respectively. Note that the barrier of 13 kcal mol^{-1} for the analogous B–H fragmentation of chemisorbed diborane (Figure S15) is slightly smaller, suggesting that chemisorbed pentaborane is somewhat less reactive than chemisorbed diborane. A reaction pathway directly connecting physisorbed pentaborane and chemisorbed B_5H_8 and H (B_5H_9:Al_{80} → B_5H_8–Al_{80}–H), with a barrier of 30 kcal mol^{-1}, was also located and is displayed in Figure S38.

B_5H_8–Al_{80}–H can undergo B–H fragmentation to form B_5H_7–Al_{80}–2H. Several conformers of the latter are shown in Figure S39, which range in energy from +8 to −15 kcal mol^{-1}. (Note that B_5H_7–Al_{80}–2H is generally more stable than chemisorbed B_5H_7 + molecular H_2, as shown by comparing Figures S39 and S40.) The structures and energies of additional multiply fragmented species B_5H_6–Al_{80}–3H, B_5H_5–Al_{80}–4H, and B_5H_4–Al_{80}–5H are shown in Figures S41–S43, but are not discussed further. Representative saddle points and IRCs for B_5H_8–Al_{80}–H → B_5H_7–Al_{80}–2H and B_5H_5–Al_{80}–4H → B_5H_4–Al_{80}–5H are displayed in Figures S44 and S45, respectively. The respective barriers are rather large, 45 and 37 kcal mol^{-1}, respectively, providing evidence that B_5H_x chemisorbed fragments of pentaborane are less susceptible to additional B–H fragmentation steps than B_2H_x fragments of diborane.

4.2.6. Formation of H_2. Because milling of Al in the presence of pentaborane again produces H_2 as the primary gaseous byproduct, an investigation of potential pathways leading to the formation of H_2 from chemisorbed B_5H_9 and some of its fragments was performed, in analogy to the reaction pathways of H_2 formation arising from chemisorbed diborane. Figures S46 and S47 show saddle points and IRCs for the unimolecular elimination of H_2 from chemisorbed pentaborane. The respective barriers for this reaction are 39 and 45 kcal mol^{-1}, substantially higher than the computed barrier of 16 kcal mol^{-1} for unimolecular H_2 elimination from chemisorbed diborane, as shown in Figure S23. A bimolecular pathway leading to the elimination of H_2 from chemisorbed B_5H_8 and H moieties, shown in Figure S48, has a barrier of 39 kcal mol^{-1}, which is somewhat larger than the corresponding barriers of 30 and 32 kcal mol^{-1} found for the elimination of H_2 from chemisorbed B_2H_5 and H (Figures S28 and S29.)

In summary, pentaborane is predicted to adsorb to aluminum surfaces but to have higher barriers, and hence slower kinetics,

DOI: 10.1021/acs.jpcc.7b03583
J. Phys. Chem. C 2017, 121, 14176–14190

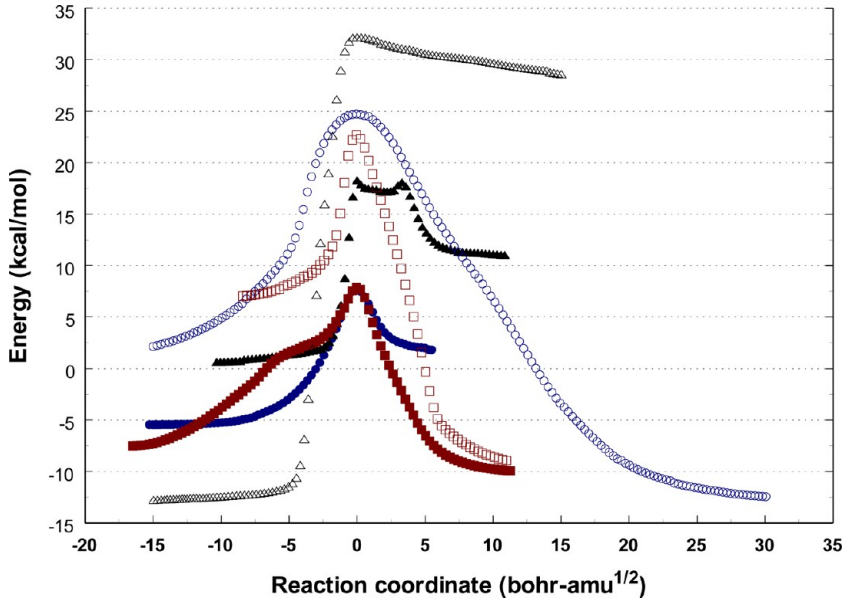

Figure 7. M06/6-311++G(d,p) intrinsic reaction coordinate (IRC) traces for chemisorption (blue circles), initial B−H fragmentation (red squares), and unimolecular elimination of H_2 (black triangles) of diborane (solid data points) and pentaborane (open data points) on the surface of the Al_{80} cluster.

for chemisorption and fragmentation compared to diborane. This might explain why substantially longer milling times were required for complete consumption of the borane fill for pentaborane compared to diborane, although the higher loading of pentaborane is presumably also a factor. DFT predicts that the kinetically favored route for the formation of H_2 in the ball milling of Al in the presence of pentaborane is chemisorption, followed by B−H fragmentation, and then recombination of chemisorbed H atoms to form H_2. The predicted barriers for pentaborane chemisorption and subsequent B−H fragmentation are 29 kcal mol^{-1} (Figure S34) and 16 kcal mol^{-1} (Figure S36), respectively. As shown in a prior study,[14] the barrier for the recombination of two chemisorbed H atoms to form H_2 is 25 kcal mol^{-1}, which is smaller than the barriers for the unimolecular (39 kcal mol^{-1}; Figure S46) and bimolecular (39 kcal mol^{-1}; Figure S48) elimination of H_2 considered in the present study.

4.2.7. Relative Energetics of Diborane and Pentaborane Reactions. The relative reactivity of diborane compared to pentaborane is illustrated in Figure 7, which is a composite plot of the lowest-barrier reaction pathways for chemisorption, initial B−H fragmentation, and unimolecular elimination of H_2. It is clear that the barriers for all three fundamental reactions are smaller for diborane than for pentaborane. This is consistent with the faster consumption of diborane observed in the ball-milling experiments.

5. CONCLUSIONS

In this work, milling of aluminum balls in boranes was shown to be an efficient method to produce boron−aluminum nanoparticles that can easily be capped to render the particles dispersible in hydrocarbons. High-resolution TEM images and EDS mapping data showed a boron-rich outer layer on an aluminum core, and mass spectrometry showed that the outer layer also contained most of the hydrogen originating from the borane reactant. XPS showed that these particles, with or without an organic capping layer, had an oxidized surface layer with an $Al_nB_oH_pO_x$ stoichiometry, but with a layer thickness (~2 nm) that was significantly lower than that of the native oxide layer that forms on bulk aluminum; that is, the boron-rich layer appears to provide partial protection against oxidation. The particles produced with pentaborane had substantially higher boron content and were also substantially more reactive upon sudden air exposure. Particle energy contents, thermal oxidation properties, and the effects of particle loading on ignition of hypergolic propellants are currently under investigation.

DFT calculations comparing the behaviors of diborane and pentaborane on the surface of Al_{80} predict diborane to be more highly reactive with aluminum than pentaborane. The barrier for chemisorption of pentaborane (29 kcal mol^{-1}) was found to be more than twice as large as that for diborane (11−12 kcal mol^{-1}). Furthermore, chemisorbed diborane undergoes unimolecular elimination of H_2 with a barrier of 16 kcal mol^{-1}, whereas the corresponding process for pentaborane has a barrier of 39 kcal mol^{-1}. In fact, for pentaborane, the kinetically preferred mechanism of H_2 generation is recombination of chemisorbed H atoms. These results are qualitatively consistent with the observed fast consumption of diborane during milling and the difference in behavior of Al milled in diborane versus pentaborane. That is, the pentaborane-milled materials retain the intrinsic explosive characteristics of pure pentaborane when exposed to air, suggesting that the pentaborane remains more intact during the milling process, apart from B−H fragmentation subsequently leading to H_2 formation.

■ ASSOCIATED CONTENT

Supporting Information

The Supporting Information is available free of charge on the ACS Publications website at DOI: 10.1021/acs.jpcc.7b03583.

Detailed discussion of the mass spectral sensitivity calibration, additional headspace mass spectra, and additional figures of the theoretical calculations (Figures S1−S46). Raw data for the graphs presented in this article (PDF)

DOI: 10.1021/acs.jpcc.7b03583
J. Phys. Chem. C 2017, 121, 14176−14190

AUTHOR INFORMATION

Corresponding Author

*Phone: 801-585-7289. E-mail: anderson@chem.utah.edu.

ORCID

Jerry A. Boatz: 0000-0002-7457-1610

Kit H. Bowen: 0000-0002-2858-6352

Scott L. Anderson: 0000-0001-9985-8178

Notes

The authors declare no competing financial interest.

ACKNOWLEDGMENTS

The Utah work was supported by the Air Force Office of Scientific Research under AFOSR Grants FA9550-12-1-0481 and FA9550-16-1-0141. XPS and STEM/EDS were performed using University of Utah shared facilities of the Micron Microscopy Suite sponsored by the College of Engineering, Health Sciences Center, Office of the Vice President for Research, and the Utah Science Technology and Research (USTAR) initiative of the State of Utah, partially supported by the MRSEC Program of the NSF under Award DMR-1121252. The STEM/EELS experiment at Argonne National Laboratory was performed by Jun Lu. A grant of computer time from the DoD High Performance Computing Modernization Program at the five DoD Supercomputing Resource Centers (DSRCs) (Air Force Research Laboratory DSRC, Army Research Laboratory DSRC, Engineer Research and Development Center DSRC, Maui High Performance Computing Center, and Navy DSRC) is gratefully acknowledged. The Johns Hopkins work was supported by an MURI grant from the Office of Naval Research (ONR) (Grant N00014-15-1-2681).

REFERENCES

(1) Ivanov, G. V.; Tepper, F. "Activated" Aluminum as a Stored Energy Source for Propellants. *Int. J. Energ. Mater. Chem. Propul.* **1997**, *4*, 636−645.

(2) Mench, M. M.; Yeh, C. L.; Kuo, K. K. Propellant Burning Rate Enhancement and Thermal Behavior of Ultra-Fine Aluminum Powders (Alex). *Int. Annu. Conf. ICT* **1998**, *29th*, 30.1−30.15.

(3) Totten, G. E., MacKenzie, S., Eds. *Handbook of Aluminum*; Marcel Decker, Inc.: New York, 2003; Vol. *1*.

(4) Galfetti, L.; Luca, L. T. D.; Severini, F.; Meda, L.; Marra, G.; Marchetti, M.; Regi, M.; Bellucci, S. Nanoparticles for Solid Rocket Propulsion. *J. Phys.: Condens. Matter* **2006**, *18*, S1991−S2005.

(5) Armstrong, R. W.; Baschung, B.; Booth, D. W.; Samirant, M. Enhanced Propellant Combustion with Nanoparticles. *Nano Lett.* **2003**, *3*, 253−255.

(6) Lynch, P.; Fiore, G.; Krier, H.; Glumac, N. Gas-Phase Reaction in Nanoaluminum Combustion. *Combust. Sci. Technol.* **2010**, *182*, 842−857.

(7) Connell, T. L., Jr.; Risha, G. A.; Yetter, R. A.; Young, G.; Sundaram, D. S.; Yang, V. Combustion of Alane and Aluminum With Water for Hydrogen and Thermal Energy Generation. *Proc. Combust. Inst.* **2011**, *33*, 1957−1965.

(8) Allen, D.; Krier, H.; Glumac, N. Heat Transfer Effects in Nano-Aluminum Combustion at High Temperatures. *Combust. Flame* **2014**, *161*, 295−302.

(9) Risha, G. A.; Son, S. F.; Yetter, R. A.; Yang, V.; Tappan, B. C. Combustion of Nano-Aluminum and Liquid Water. *Proc. Combust. Inst.* **2007**, *31*, 2029−2036.

(10) Yetter, R. A.; Risha, G. A.; Son, S. F. Metal Particle Combustion and Nanotechnology. *Proc. Combust. Inst.* **2009**, *32*, 1819−1838.

(11) Sundaram, D. S.; Yang, V.; Huang, Y.; Risha, G. A.; Yetter, R. A. Effects of Particle Size and Pressure on Combustion of Nano-Aluminum Particles and Liquid Water. *Combust. Flame* **2013**, *160*, 2251−2259.

(12) Wang, H.; Jian, G.; Yan, S.; DeLisio, J. B.; Huang, C.; Zachariah, M. R. Electrospray Formation of Gelled Nano-Aluminum Microspheres with Superior Reactivity. *ACS Appl. Mater. Interfaces* **2013**, *5*, 6797−6801.

(13) Campbell, T.; Kalia, R. K.; Nakano, A.; Vashishta, P.; Ogata, S.; Rodgers, S. Dynamics of Oxidation of Aluminum Nanoclusters using Variable Charge Molecular-Dynamics Simulations on Parallel Computers. *Phys. Rev. Lett.* **1999**, *82*, 4866−4869.

(14) McMahon, B. W.; Perez, J. P. L.; Yu, J.; Boatz, J. A.; Anderson, S. L. Synthesis of Nanoparticles from Malleable and Ductile Metals Using Powder-Free, Reactant-Assisted Mechanical Attrition. *ACS Appl. Mater. Interfaces* **2014**, *6*, 19579−19591.

(15) McMahon, B. W.; Yu, J.; Boatz, J. A.; Anderson, S. L. Rapid Aluminum Nanoparticle Production by Milling in NH_3 and CH_3NH_2 Atmospheres: An Experimental and Theoretical Study. *ACS Appl. Mater. Interfaces* **2015**, *7*, 16101−16116.

(16) Yu, J.; McMahon, B. W.; Boatz, J. A.; Anderson, S. L. Aluminum Nanoparticle Production by Acetonitrile-Assisted Milling: The Effects of Liquid vs. Vapor Phase Milling, and of Milling Method on Particle Size and Surface Chemistry. *J. Phys. Chem. C* **2016**, *120*, 19613−19629.

(17) Perez, J. P. L.; McMahon, B. W.; Yu, J.; Schneider, S.; Boatz, J. A.; Hawkins, T. W.; McCrary, P. D.; Flores, L. A.; Rogers, R. D.; Anderson, S. L. Boron Nanoparticles with High Hydrogen Loading: Mechanism for B−H Binding and Potential for Improved Combustibility and Specific Impulse. *ACS Appl. Mater. Interfaces* **2014**, *6*, 8513−8525.

(18) Perez, J. P. L.; Yu, J.; Sheppard, A. J.; Chambreau, S. D.; Vaghjiani, G. L.; Anderson, S. L. Binding of Alkenes and Ionic Liquids to B−H Functionalized Boron Nanoparticles: Creation of Particles with Controlled Dispersibility and Minimal Surface Oxidation. *ACS Appl. Mater. Interfaces* **2015**, *7*, 9991−10003.

(19) Wirth, H. E.; Palmer, E. D. Dielectric Constant and Vapor Pressure of Pentaborane. *J. Phys. Chem.* **1956**, *60*, 914−916.

(20) Zhao, Y.; Truhlar, D. G. The M06 Suite of Density Functionals for Main Group Thermochemistry, Thermochemical Kinetics, Noncovalent Interactions, Excited States, and Transition Elements: Two New Functionals and Systematic Testing of Four M06-Class Functionals and 12 Other Functionals. *Theor. Chem. Acc.* **2008**, *120*, 215−241.

(21) McLean, A. D.; Chandler, G. S. Contracted Gaussian Basis Sets for Molecular Calculations. I. Second Row Atoms, Z = 11−18. *J. Chem. Phys.* **1980**, *72*, 5639−5648.

(22) Francl, M. M.; Pietro, W. J.; Hehre, W. J.; Binkley, J. S.; Gordon, M. S.; DeFrees, D. J.; Pople, J. A. Self-Consistent Molecular Orbital Methods. XXIII. A Polarization-Type Basis Set for Second-Row Elements. *J. Chem. Phys.* **1982**, *77*, 3654−3665.

(23) Clark, T.; Chandrasekhar, J.; Spitznagel, G. W.; Schleyer, P. v. R. Efficient Diffuse Function-Augmented Basis Sets for Anion Calculations. III. The 3-21+G Basis Set for First-Row Elements, Li-F. *J. Comput. Chem.* **1983**, *4*, 294−301.

(24) Krishnan, R.; Binkley, J. S.; Seeger, R.; Pople, J. A. Self-Consistent Molecular Orbital Methods. XX. A Basis Set for Correlated Wave Functions. *J. Chem. Phys.* **1980**, *72*, 650−654.

(25) Gonzalez, C.; Schlegel, H. B. An Improved Algorithm for Reaction Path Following. *J. Chem. Phys.* **1989**, *90*, 2154−2161.

(26) Schmidt, M. W.; Baldridge, K. K.; Boatz, J. A.; Elbert, S. T.; Gordon, M. S.; Jensen, J. H.; Koseki, S.; Matsunaga, N.; Nguyen, K. A.; Su, S.; et al. A General Atomic and Molecular Electronic Structure System. *J. Comput. Chem.* **1993**, *14*, 1347−1363.

(27) Gordon, M. S.; Schmidt, M. W. Advances in Electronic Structure Theory: GAMESS a Decade Later. In *Theory and Applications of Computational Chemistry: The First Forty Years*; Dykstra, C., Frenking, G., Kim, K. S., Scuseria, G. E., Eds.; Elsevier: Amsterdam, 2005; Chapter 41, pp 1167−1190.

(28) Stein, S. E. Mass Spectra and IR Spectra. In *NIST Chemistry WebBook, NIST Standard Reference Database 69*; Linstrom, P. J., Mallard, W. G., Eds.; NIST Mass Spec Data Center, National Institute

DOI: 10.1021/acs.jpcc.7b03583
J. Phys. Chem. C 2017, 121, 14176−14190

of Standards and Technology: Gaithersburg, MD, February 2000; http://webbook.nist.gov.
(29) Norton, F. J. The Mass Spectrum of Monoisotopic $^{10}B_2H_6$. *J. Am. Chem. Soc.* **1949**, *71*, 3488−3491.
(30) Margrave, J. L. A Mass Spectrometric Appearance Potential Study of Diborane. *J. Phys. Chem.* **1957**, *61*, 38−41.
(31) Basner, R.; Schmidt, M.; Becker, K. Absolute Total and Partial Cross Sections for the Electron Impact Ionization of Diborane (B_2H_6). *J. Chem. Phys.* **2003**, *118*, 2153−2158.
(32) Van Devener, B.; Perez, J. P. L.; Anderson, S. L. Air-Stable, Unoxidized, Fuel-Soluble Boron Nanoparticles. *J. Mater. Res.* **2009**, *24*, 3462−3464.
(33) Dias, A. M. A.; Bonifacio, R. P.; Marrucho, I. M.; Padua, A. A. H.; Costa Gomes, M. F. Solubility of oxygen in n-hexane and in n-perfluorohexane. Experimental determination and prediction by molecular simulation. *Phys. Chem. Chem. Phys.* **2003**, *5*, 543−549.
(34) Cliff, G.; Lorimer, G. W. The Quantitative Analysis of Thin Specimens. *J. Microsc.* **1975**, *103*, 203−207.
(35) Moulder, J. F., Stickle, W. F., Sobol, P. E., Bomben, K. D. *Handbook of X-ray Photoelectron Spectroscopy: A Reference Book of Standard Spectra for Identification and Interpretation of XPS Data*; Chastain, J., King, R. C., Jr., Eds.; Physical Electronics: Eden Prarie, MN, 1995.
(36) Naumkin, A. V.; Kraut-Vass, A.; Gaarenstroom, S. W.; Powell, C. J. *NIST X-ray Photoelectron Spectroscopy Database, NIST Standard Reference Database 20*, version 4.1; National Institute of Standards and Technology: Gaithersburg, MD, 2012; http://srdata.nist.gov/xps/.
(37) Kloprogge, J. T.; Duong, L. V.; Wood, B. J.; Frost, R. L. XPS Study of The Major Minerals in Bauxite: Gibbsite, Bayerite and (Pseudo-) Boehmite. *J. Colloid Interface Sci.* **2006**, *296*, 572−576.
(38) Balchev, I.; Minkovski, N.; Marinova, T.; Shipochka, M.; Sabotinov, N. Composition and Structure Characterization of Aluminum after Laser Ablation. *Mater. Sci. Eng., B* **2006**, *135*, 108−112.
(39) Schoser, S.; Bräuchle, G.; Forget, J.; Kohlhof, K.; Weber, T.; Voigt, J.; Rauschenbach, B. XPS Investigation of AlN Formation in Aluminum Alloys Using Plasma Source Ion Implantation. *Surf. Coat. Technol.* **1998**, *103−104*, 222−226.
(40) Moulder, J. F.; Stickle, W. F.; Sobol, P. E.; Bomben, K. D. *Handbook of X-ray Photoelectron Spectroscopy: A Reference Book of Standard Spectra for Identification and Interpretation of XPS Data*; Chastain, J., Ed.; Perkin-Elmer Corporation: Eden Prairie, 1992.
(41) Zähr, J.; Oswald, S.; Türpe, M.; Ullrich, H. J.; Füssel, U. Characterisation of Oxide and Hydroxide Layers on Technical Aluminum Materials Using XPS. *Vacuum* **2012**, *86*, 1216−1219.
(42) Baker, C. C.; Ceylan, A.; Shah, S. I. Reactive Gas Condensation Synthesis of Aluminum Nitride Nanoparticles. *J. Nanosci. Nanotechnol.* **2006**, *6*, 146−150.
(43) Kwon, Y.-S.; Gromov, A. A.; Ilyin, A. P.; Rim, G.-H. Passivation Process for Superfine Aluminum Powders Obtained by Electrical Explosion of Wires. *Appl. Surf. Sci.* **2003**, *211*, 57−67.
(44) Davies, P. R.; Newton, N. G. The Chemisorption and Decomposition of Pyridine and Ammonia at Clean and Oxidised Al(111) Surfaces. *Surf. Sci.* **2003**, *546*, 149−158.
(45) Powell, C. J.; Jablonski, A. *NIST Electron Effective-Attenuation-Length Database, NIST Standard Reference Database 82*, version 1.3; National Institute of Standards and Technology: Gaithersburg, MD, 2011.
(46) Baer, D. R.; Engelhard, M. H. XPS Analysis of Nanostructured Materials and Biological Surfaces. *J. Electron Spectrosc. Relat. Phenom.* **2010**, *178−179*, 415−432.
(47) Van Devener, B.; Perez, J. P. L.; Jankovich, J.; Anderson, S. L. Oxide-Free, Catalyst-Coated, Fuel-Soluble, Air-Stable Boron Nanopowder as Combined Combustion Catalyst and High Energy Density Fuel. *Energy Fuels* **2009**, *23*, 6111−6120.
(48) Sheasby, P. G.; Pinner, R. *The Surface Treatment and Finishing of Aluminium and Its Alloys*, 6th ed.; ASM International: Materials Park, OH, 2001.
(49) Mangolini, F.; McClimon, J. B.; Rose, F.; Carpick, R. W. Accounting for Nanometer-Thick Adventitious Carbon Contamination in X-ray Absorption Spectra of Carbon-Based Materials. *Anal. Chem.* **2014**, *86*, 12258−12265.
(50) Chung, S. W.; Guliants, E. A.; Bunker, C. E.; Hammerstroem, D. W.; Deng, Y.; Burgers, M. A.; Jelliss, P. A.; Buckner, S. W. Capping and Passivation of Aluminum Nanoparticles Using Alkyl-Substituted Epoxides. *Langmuir* **2009**, *25*, 8883−8887.
(51) Baláž, P.; Achimovičová, M.; Baláž, M.; Billik, P.; Cherkezova-Zheleva, Z.; Criado, J. M.; Delogu, F.; Dutková, E.; Gaffet, E.; Gotor, F. J.; et al. Hallmarks of Mechanochemistry: From Nanoparticles to Technology. *Chem. Soc. Rev.* **2013**, *42*, 7571−7637.

DOI: 10.1021/acs.jpcc.7b03583
J. Phys. Chem. C 2017, 121, 14176−14190